Supplementary Information

Hydrogen production based on photoactivated nanowire-forest

*Seyeong Le[§a], Zahid Hagnif[§a], Keumyoung Seo[b], Taekyung Lim[b], Hye-Min Shin[a], Sungjun Park[a], Su Hwan Kim[c], Sang Kyu Kwak[cd], Sukwon Hong[e], Myung-Han Yoon[*a], Sanghyun Ju[*b]*

[a]School of Materials Science and Engineering, Gwangju Institute of Science and Technology, 123 Cheomdan-gwagiro, Buk-gu, Gwangju 61005, Republic of Korea

[b]Department of Physics, Kyonggi University, Suwon, Gyeonggi-Do 16227, Republic of Korea

[c]School of Energy and Chemical Engineering, Ulsan National Institute of Science and Technology (UNIST), Ulsan 44919, Republic of Korea

[d]Center for Multidimensional Carbon Materials, Institute for Basic Science (IBS), Ulsan 44919, Republic of Korea

[e]Department of Chemistry, Gwangju Institute of Science and Technology, Gwangju 61005, Republic of Korea

[§]These authors contributed equally to this work.

[*]To whom correspondence should be addressed.

E-mail: mhyoon@gist.ac.kr, shju@kgu.ac.kr

S1. Structure characterization of Iron oxide nanoparticles

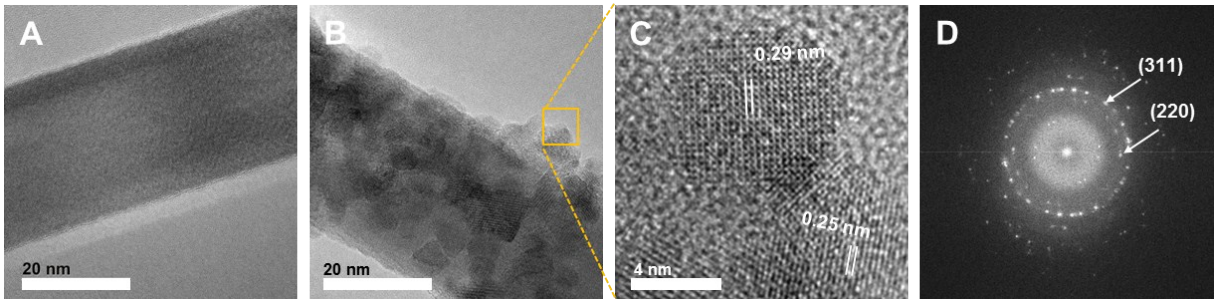

Figure S1 | TEM images of (**A**) SnO_2 nanowire and (**B**) iron oxide nanoparticle coated SnO_2 nanowire. (**C**) HR-TEM image of iron oxide nanoparticles and (**D**) the corresponding diffraction pattern.

The HR-TEM images show that most of SnO_2 nanowires were conformally covered by polycrystalline iron oxide nanostructures, with an average size of 10 nm. Furthermore, the iron oxide nanostructures show lattice fringes with interfringe distances of 0.29 nm and 0.25 nm, which are close to the interplanar distances of the (220) and (311) planes respectively. These heterostructures were prepared by a simple process, consisting of dipping the substrate in an aqueous solution of iron chloride salts. This suggests that the SnO_2 nanowire forest grown on nickel foam can successfully function as a nanoscale scaffold for the uniform coating of solution-deposited iron oxide nanostructures, and thereby substantially increase the effective surface area for catalytic reaction with water vapor, as compared with the bare nickel foam.

S2. Chemical characterization

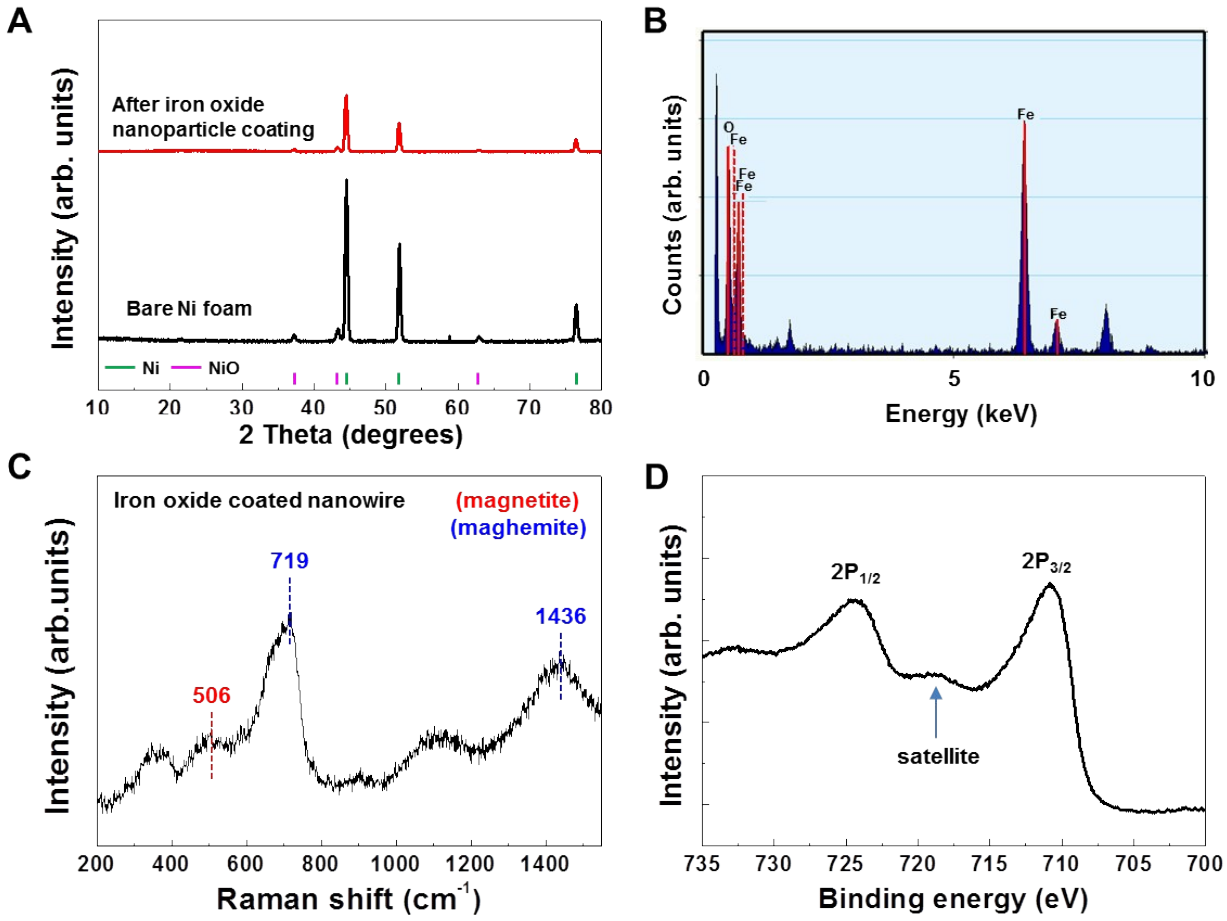

Figure S2 | (**A**) XRD pattern of bare Ni foam and iron-oxide-nanoparticle-coated Ni foam prepared *via* a co-precipitation method. (**B**) EDX spectrum of iron oxide nanoparticles. (**C**) Raman spectrum of iron-oxide-coated Ni/SnO_2 3D scaffold. (**D**) Fe 2p XPS spectrum of the iron-oxide-coated Ni/SnO_2 3D scaffold.

X-ray diffraction (XRD) was conducted to identify the regularly spaced atoms of the synthesized iron oxide crystal structure. Figure S2A shows the XRD peaks of the Ni foam before and after coating with iron oxide nanoparticles. The diffraction peaks of the bare Ni foam are the same as those observed in the iron-nanoparticle-coated Ni foam. The XRD results reveal no evidence of a crystalline iron oxide nanoparticle phase. The crystal structure of the synthesized iron oxide nanoparticles was estimated to be

amorphous or polycrystalline before the annealing step. The diffraction peaks represent Ni and NiO in the 3D scaffold and correspond to JCPDS# 01–1260 and 78–0429, respectively.

Energy-dispersive X-ray spectrometry (EDX) mapping was performed to confirm the elemental composition of the iron oxide nanoparticles (Figure S2B). The EDX spectrum displays Fe and O peaks for the iron oxide nanoparticles. Distinguishing the magnetite and haemaite phases of iron oxide is difficult because these two phases are very similar; thus, the presence of haematite or another phase cannot be excluded on the basis of the XRD results alone. The iron oxide coating method is based on a solution process, which facilitates uniform nanoparticle coating on the complex 3D scaffolds. Figure S2C shows the Raman spectrum of the iron-oxide-coated Ni/SnO_2 3D scaffold. The red line corresponds to the magnetite (Fe_3O_4) peak, and the blue line corresponds to the maghemite (γ-Fe_2O_3) peaks. The Raman spectra of the nanoparticles synthesized by co-precipitation show broad bands at approximately 506 and 719 cm^{-1} with shoulder peaks.[1]

Additionally, to confirm the chemical composition of the iron oxide-coated 3D scaffold, we collected the Fe 2p X-ray photoelectron spectra (Figure S2D). The binding energies of Fe 2p1/2 and Fe 2p3/2 are 710.8 eV and 724.6 eV, respectively. The position of the satellite peak corresponds to maghemite. The positions of the Fe 2p and satellite peaks are related to the oxidation states of iron oxide. This result indicates that the synthesized iron oxide nanoparticles have a multivalent oxidation state.

S3. Brunauer-Emmett-Teller (BET) analysis

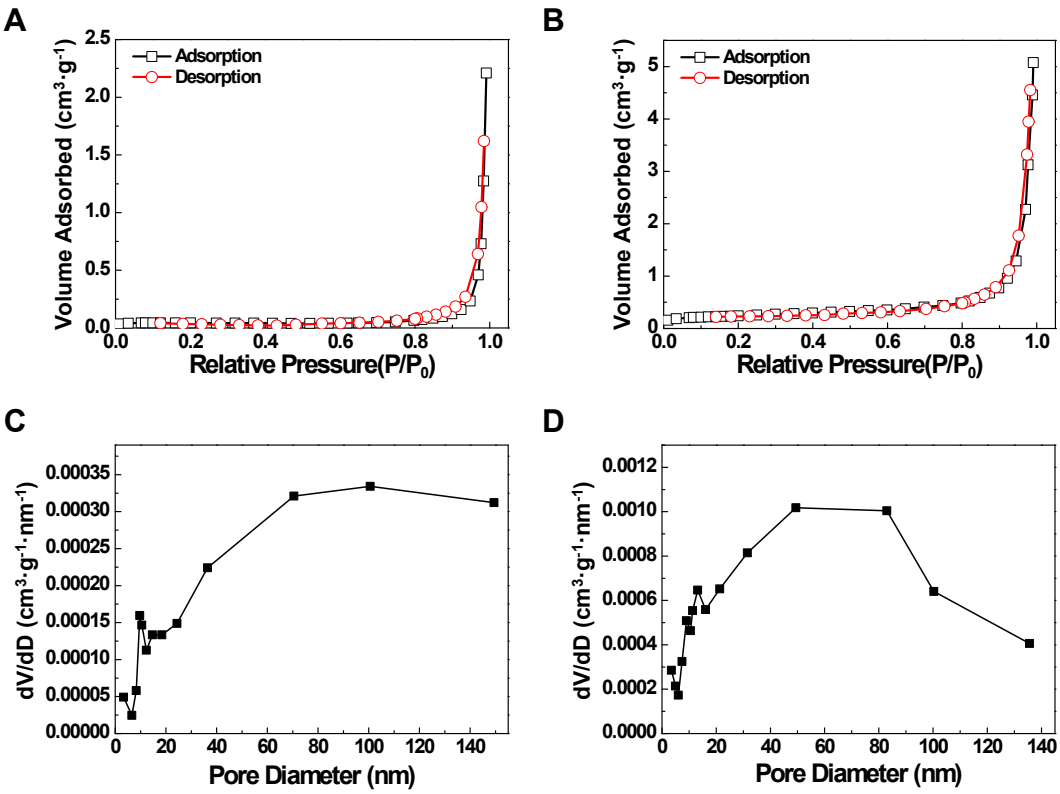

Figure S3 | Nitrogen adsorption-desorption isotherms (**A, B**) and the corresponding BJH pore size distributions (**C, D**) of the bare (**A, C**) and nanowire-grown nickel foams (**B, D**).

The measured Brunauer-Emmett-Teller (BET) areas of the bare and nanowire-grown nickel foams are 0.1812 and 0.8609 $m^2 \cdot g^{-1}$, respectively. These results indicate that the surface area available for depositing iron oxide nanoparticles is significantly increased as compared to the bare nickel foam.

S4. Measurement of UV-vis spectroscopy

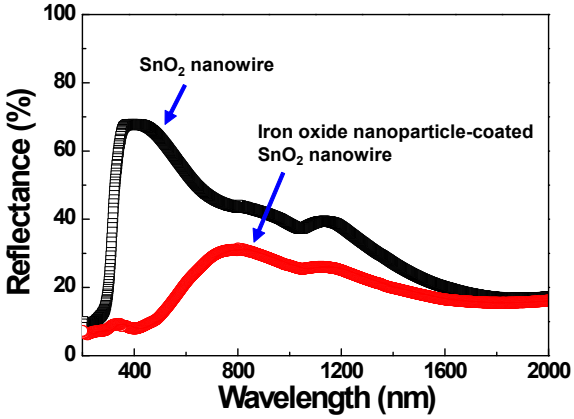

Figure S4 | UV-vis reflectance spectra of SnO_2 nanowire forest on SiO_2 before and after the solution-based deposition of iron oxide nanoparticles following the same experimental procedure.

The optical properties of the iron oxide nanoparticles are also important for the evaluation of its optical and photocatalytic activity. The UV-vis spectra were obtained in the reflection mode in the 200 – 2000 nm range of wavelengths. Figure S4 clearly indicates that the UV light absorption substantially increased after the deposition of iron oxide nanoparticles. Therefore, iron oxide nanoparticles are responsible for DUV absorption and, thereby, photochemical regeneration of oxygen vacancies, leading to the regeneration of reactive sites on the iron oxide nanocoating.

S5. Hydrogen generation system and generation over time

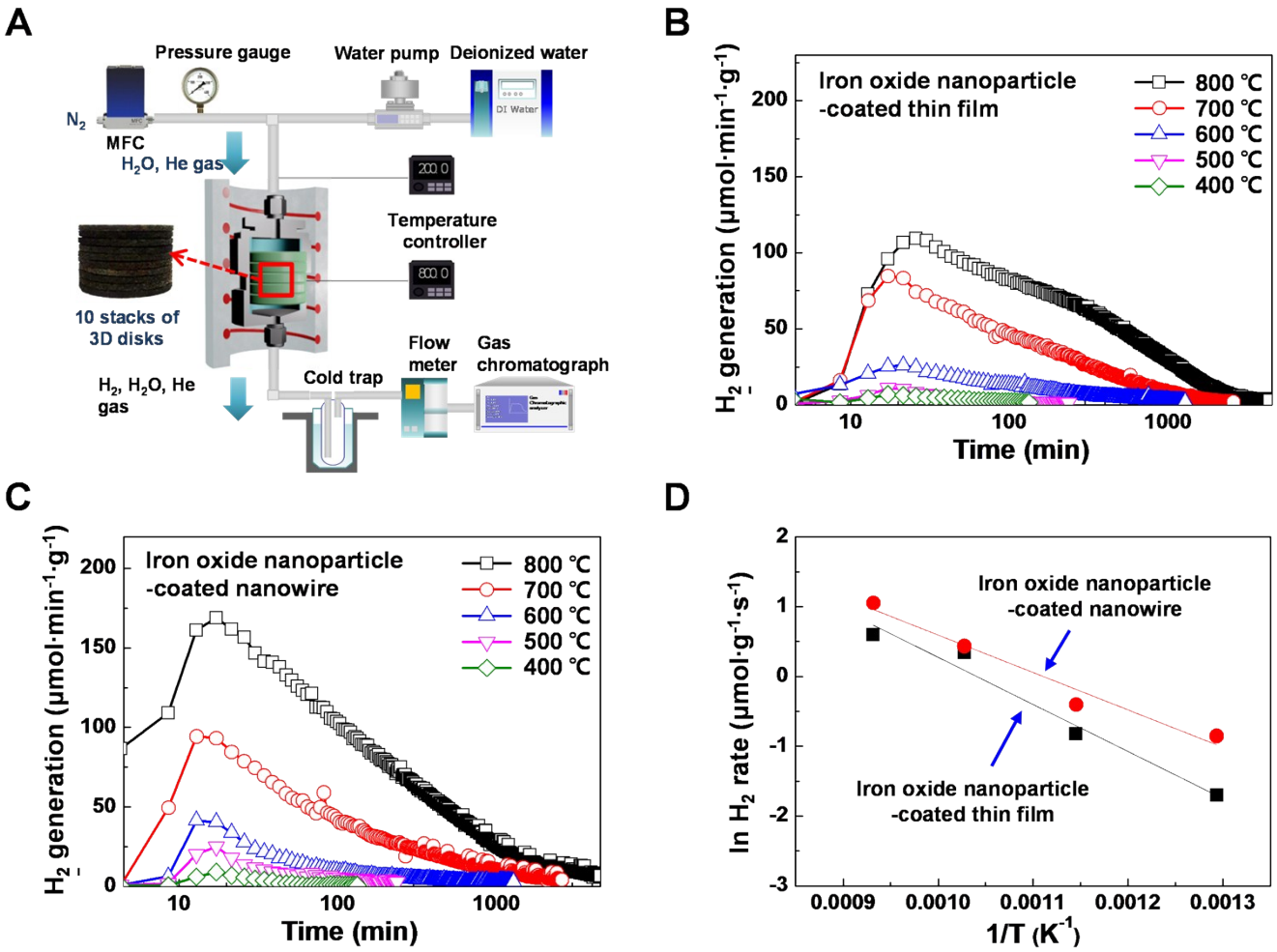

Figure S5 | (**A**) Experimental setup for hydrogen generation. (**B, C**) Changes in the rate of H_2 generation with time at various temperatures (400–800 °C in 100 °C increments). H_2 generation results for (**B**) 3D porous disks covered with an iron oxide thin film, and (**C**) 3D porous disks covered with iron oxide-coated SnO_2 nanowires. (**D**) Arrhenius plots of the hydrogen production rates.

Figure S5 shows the time profiles for H_2 generation at different reactor temperatures. The amount and rate of H_2 generation increased with increasing temperature. At each specific temperature, the instantaneous H_2 generation was remarkably enhanced during the first 20 min, followed by a decrease. The total amount of H_2 generated on the iron-oxide-coated nanowire forest (iron-oxide-nanoparticle-

coated thin films), obtained by integrating the profiles of the H_2 generation rate *versus* time, was 263.3 (421.4) μmol·g^{-1} at 400 °C, 2,036.5 (672.7) μmol·g^{-1} at 500 °C, 6,094.0 (6,987.9) μmol·g^{-1} at 600 °C, 33,216.6 (29,459.1) μmol·g^{-1} at 700 °C, and 98,731.2 (83,024.8) μmol·g^{-1} at 800 °C.

The kinetic investigation for the water-splitting step at different temperatures (500–800 °C) was based on a zero-order approximation. Figure S5D is a plot of two Arrhenius curves from the water-splitting step with the iron oxide-coated Ni foam and iron oxide-coated-nanowire-grown Ni foam. The rate constant is given by the Arrhenius equation as $r = k_0 e^{-(Ea/RT)}$, where r is the reaction rate (μmol·g^{-1}·s^{-1}), k_0 is the reaction constant (μmol·g^{-1}·s^{-1}), E_a is the activation energy for the reaction, R is the gas constant, and T is the reaction temperature (K). The reaction rate is faster at higher temperatures, demonstrating a linear relationship with the reaction temperature. From the slope of the straight line in the Arrhenius plots, the activation energy was calculated to be 56.1 kJ·mol^{-1} and 44.6 kJ·mol^{-1} for the iron oxide-coated Ni foam and iron oxide-coated-nanowire-grown Ni foam, respectively.

S6. FE-SEM images of iron-oxide-coated nanowire forests and thin films before and after hydrogen generation

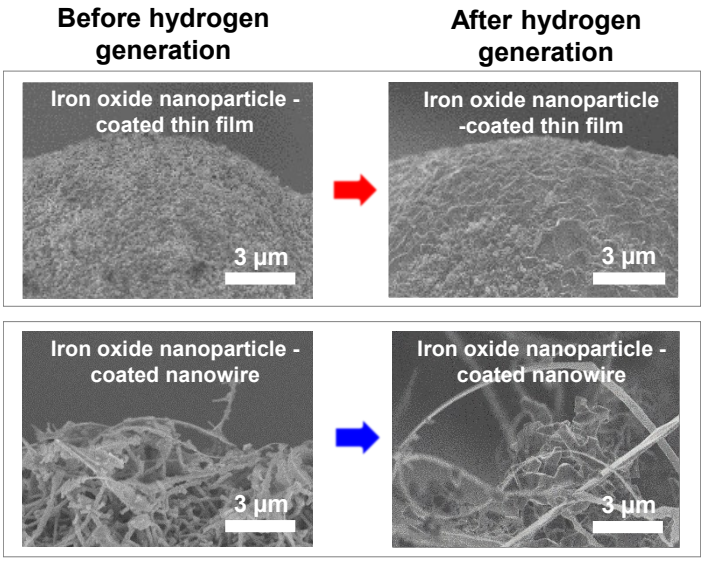

Figure S6 | Hydrogen generation with iron-oxide-coated nanowire forest and thin films. FE-SEM images of the iron oxide morphology before and after the water-splitting process.

S7. Geometrically optimized Fe_3O_4 systems

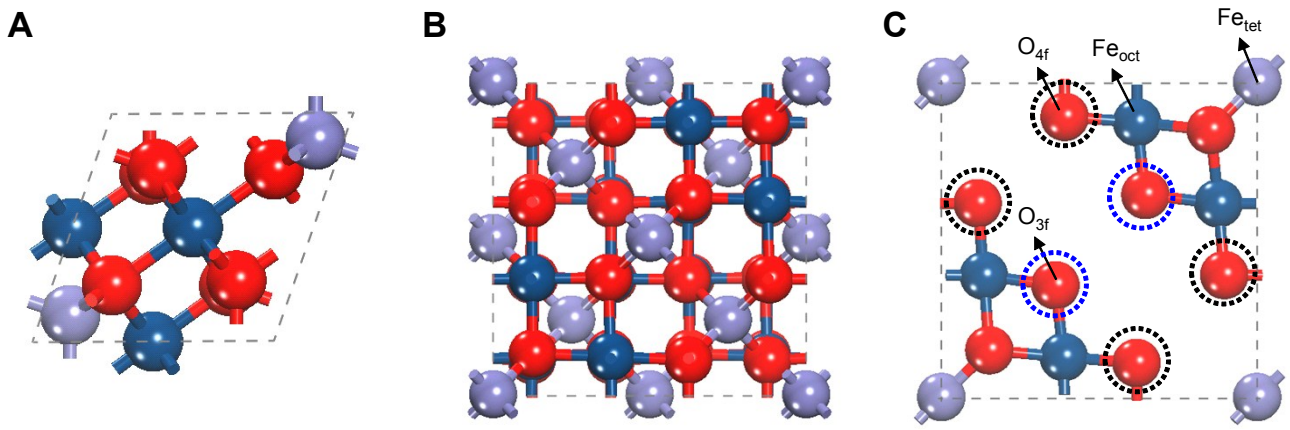

Figure S7 | Bulk unit cells of Fe_3O_4 and the Fe_3O_4 (001) surface of the $(\sqrt{2} \times \sqrt{2})R45°$ unit cell (top view). (**A**) Primitive unit cell of Fe_3O_4. (**B**) Cubic unit cell of Fe_3O_4. (**C**) Top view of the (001) surface slab (only showing the top layer). Fe_{oct}, Fe_{tet} and O are coloured navy blue, light purple and red, respectively. Dashed black circles indicate 4-fold oxygen (O_{4f}), and blue dashed circles indicate 3-fold oxygen (O_{3f}).

S8. Summary of the metal-oxide-based two-step thermochemical

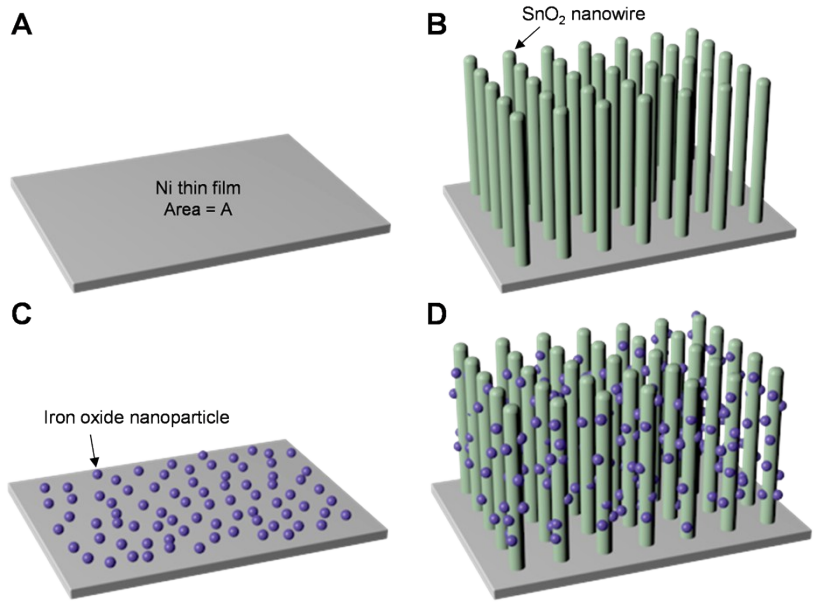

Figure S8 | Schematic representations of the hierarchically-organized structures: (**A**) nickel thin film, (**B**) SnO_2 nanowire forest on the nickel thin film, (**C**) nickel thin film coated with iron oxide nanoparticles, and (**D**) the SnO_2 nanowire forest coated with iron oxide nanoparticles.

Figure S8 shows that the nanowire forest allows a significant increase in surface area for loading iron oxide nanoparticles, and help to prevent these nanoparticles from coalescing. The HR-TEM image included with this response letter shows that most of SnO_2 nanowires were conformally covered by iron oxide nanostructures without irregular aggregation. This result clearly indicates that the SnO_2 nanowire forest grown on nickel foam successfully functions as a nanoscale scaffold for the uniform coating of iron oxide nanostructures. This increases the effective surface area for catalytic reaction with water vapor, as compared with bare nickel foam. As a result, the efficiency of hydrogen formation at the nanowire-forest scaffold was higher than that at the bare scaffold by 1.5 times. Finally, such a hierarchically organized structure of iron oxide nanomaterials on the rigid nanowire-modified microporous scaffold contributes to the retention of iron oxide nanostructures even after multiple reaction cycles at elevated temperatures, without the collapse of the nanostructured catalyst particles.

S9. Summary of the metal-oxide-based two-step thermochemical water-splitting cycle

Table S1. General comparison between current metal-oxide-based two-step thermochemical cycles

Total amount of hydrogen ($mmol \cdot g^{-1}$)	Max. hydrogen generation ($mmol \cdot min^{-1} \cdot g^{-1}$)	Generation time (min)	Reaction temperature (°C)	Materials
450	18	60	1400	ZrO_2-supported $NiFe_2O_4$ [2]
315.2		25	900	Mn ferrite [3]
500	15.6	111	1000	$CoFe_2O_4$ [4]
83.9		40	900	$Sn_xFe_yO_z$ [5]
4154.5	2334	2	600	$CoFe_XO_4$ [6]
140	0.834	16.7	1100	Ni ferrite [7]
428	9.9	16.7	1100	Ni ferrite [8]
4332	222	16.7	1100	Co ferrite zirconia [9]
102	33	25	1350	Hercynite ($FeAl_2O_4$) [10]
178.6	138.4	10	800	Ceria [11]
232.1	4.9	60	1000	Fe-YSZ [12]
401.8	25	60	800	LaSrMnO perovskites [13]
1188.2	320	30	900	CeO_2 [14]
25,401.9	**175**	**250**	**800**	**This work**

We compared the total amount of generated hydrogen and the generation time of our iron-oxide-based device with values previously reported for other metal-oxide-based materials, as summarized in Table S1. The aforementioned thermochemical cycle is a two-step water-splitting reaction to generate hydrogen. Most of these systems have hydrogen generation times shorter than 60 min. However, our results show a long generation time and a large amount of total hydrogen generated.

S10. XPS survey spectrum of iron oxide after DUV reduction

Table S2. Peak-fitting results (full-width at half-maximum (FWHM) and % area) of Fe 2p and O 1s peaks as a function of DUV irradiation.[15]

Fe 2p peak

Before DUV	KE (eV)	FWHM (eV)	Rel. area %
Fe^{2+} ($2p_{(3/2)}$)	709.7	2.21	**12.00%**
Fe^{3+} ($2p_{(3/2)}$)	711.1	3.17	34.80%
Fe^{2+} ($2p_{(3/2)}$) - satellites	714.5	4.15	24.20%
Fe^{3+} ($2p_{(3/2)}$) - satellites	719	4.11	8.80%
Fe^{2+} ($2p_{(1/2)}$)	723.3	2.57	5.70%
Fe^{3+} ($2p_{(1/2)}$)	724.7	3.76	14.50%
After DUV	KE (eV)	FWHM (eV)	Rel. area %
Fe^{2+} ($2p_{(3/2)}$)	709.7	2.91	**28.20%**
Fe^{3+} ($2p_{(3/2)}$)	711.1	3.69	35.20%
Fe^{2+} ($2p_{(3/2)}$) - satellites	714.5	4.57	18.00%
Fe^{3+} ($2p_{(3/2)}$) - satellites	719	2.72	2.60%
Fe^{2+} ($2p_{(1/2)}$)	723.3	3.19	11.60%
Fe^{3+} ($2p_{(1/2)}$)	724.7	2.95	4.30%

O 1s peak

Before DUV	KE (eV)	FWHM (eV)	Rel. area %
M–O–M	530.1	1.62	60.20%
OH–L	531.6	1.23	15.40%
OH_{ad}	532.1	1.83	**23.90%**
Water	533.3	1.36	0.50%
After DUV	KE (eV)	FWHM (eV)	Rel. area %
M–O–M	530.1	1.61	46.40%
OH–L	531.6	1.82	28.20%
OH_{ad}	532.1	1.39	**17.80%**
Water	533.3	1.36	7.60%

A comparison of the Fe 2p peaks of iron oxide before and after DUV irradiation shows that the relative concentration of Fe^{2+} increases after DUV exposure. On the basis of the quantitative results for the O 1s peak, the relative concentration of OH adsorbed onto the surface of iron oxide decreases after DUV exposure.

S11. Formation energy of oxygen vacancies and Fermi energy of bulk Fe_3O_4

Table S3. Vacancy formation energy of the (001) surface and bulk system. V_{O4f} and V_{O3f} indicate vacancies of O_{4f} and O_{3f}, respectively.

	$Fe_3O_4(001)$-V_{O4f}	$Fe_3O_4(001)$-V_{O3f}	Bulk
V_o	2.351	2.111	2.927
V_o^+	1.858	1.692	10.191
V_o^{++}	1.365	1.272	17.454
E_F^{vac}	-0.493	-0.419	7.264

The vacancy formation energies of O_{4f} and O_{3f} on the (001) surface are smaller than those of the bulk system for both neutral and charged vacancies. For the thin-layer system (the (001) surface-slab system), the formation of charged vacancies is preferred, whereas that for the bulk is disfavoured because of its positive Fermi energy.

References

1. I. Chourpa, L. Douziech-Eyrolles, L. Ngaboni-Okassa, J. F. Fouquenet, S. Cohen-Jonathan, M. Soucé, H. Marchais and P. Dubois, *The Analyst,* 2005, **130,** 1395–1403.

2. N. Gokon, H. Murayama, A. Nagasaki and T. Kodama, *Sol. Energy,* 2009, **83,** 527–537.

3. R. R. Bhosale, R. V. Shende and J. A. Puszynski, *Int. J. Hydrog. Energy,* 2012, **37,** 2924–2934.

4. J. R. Scheffe, J. Li and A. W. Weimer, *Int. J. Hydrog. Energy,* 2010, **35,** 3333–3340.

5. R. Bhosale, R. Khadka, J. Puszynski and R. Shende, *J. Renew. Sustain. Energy,* 2011, **3,** 063104.

6. J. R. Scheffe, M. D. Allendorf, E. N. Coker, B. W. Jacobs, A. H. McDaniel and A. W. Weimer, *Chem. Mater.,* 2011, **23,** 2030–2038.

7. C. Agrafiotis, A. Zygogianni, C. Pagkoura, M. Kostoglou and A. G. Konstandopoulos, *AIChE J.,* 2013, **59,** 1213–1225.

8. M. Kostoglou, S. Lorentzou and A. G. Konstandopoulos, *Int. J. Hydrog. Energy,* 2014, **39,** 6317–6327.

9. J. R. Scheffe, A. H. McDaniel, M. D. Allendorf and A. W. Weimer, *Energy Environ. Sci.,* 2013, **6,** 963–973.

10. C. L. Muhich, B. W. Evanko, K. C. Weston, P. Lichty, X. Liang, J. Martinek, C. B. Musgrave and A. W. Weimer, *Science,* 2013, **341,** 540–542.

11. W. C. Chueh, C. Falter, M. Abbott, D. Scipio, P. Furler, S. M. Haile and A. Steinfeld, *Science,* 2010, **330,** 1797–1801.

12. N. Gokon, T. Hasegawa, S. Takahashi and T. Kodama, *Energy,* 2008, **33,** 1407–1416.

13. C.-K. Yang, Y. Yamazaki, A. Aydin and S. M. Haile, *J. Mater. Chem. A,* 2014, **2,** 13612–13623.

14. J. T. Jang, K. J. Yoon and G. Y. Han, *Sol. Energy,* 2014, **101,** 29–39.

15. T.-C. Lin, G. Seshadri and J. A. Kelber, *Appl. Surf. Sci.,* 1997, **119,** 83–92.